



Cite this: *Nanoscale*, 2015, 7, 10438

## Band edge engineering of TiO<sub>2</sub>@DNA nanohybrids and implications for capacitive energy storage devices†

Roghayeh Imani,<sup>a,b</sup> Meysam Pazoki,<sup>c</sup> Ashutosh Tiwari,<sup>\*d,e</sup> G. Boschloo,<sup>c</sup> Anthony P. F. Turner,<sup>d</sup> V. Kralj-Iglic<sup>b</sup> and Aleš Iglič<sup>\*a</sup>

Novel mesoporous TiO<sub>2</sub>@DNA nanohybrid electrodes, combining covalently encoded DNA with mesoporous TiO<sub>2</sub> microbeads using dopamine as a linker, were prepared and characterised for application in supercapacitors. Detailed information about donor density, charge transfer resistance and chemical capacitance, which have an important role in the performance of an electrochemical device, were studied by electrochemical methods. The results indicated the improvement of electrochemical performance of the TiO<sub>2</sub> nanohybrid electrode by DNA surface functionalisation. A supercapacitor was constructed from TiO<sub>2</sub>@DNA nanohybrids with PBS as the electrolyte. From the supercapacitor experiment, it was found that the addition of DNA played an important role in improving the specific capacitance (C<sub>s</sub>) of the TiO<sub>2</sub> supercapacitor. The highest C<sub>s</sub> value of 8 F g<sup>-1</sup> was observed for TiO<sub>2</sub>@DNA nanohybrids. The nanohybrid electrodes were shown to be stable over long-term cycling, retaining 95% of their initial specific capacitance after 1500 cycles.

Received 19th April 2015,  
Accepted 5th May 2015  
DOI: 10.1039/c5nr02533h

www.rsc.org/nanoscale

### Introduction

Electrochemical supercapacitors are a new class of energy storage devices, which are attracting considerable interest due to their high power density, long cycle life and short charging time.<sup>1</sup> The important factors affecting the performance of supercapacitors are the intrinsic properties of electrode materials and electrolyte, architecture of the device and the fabrication methods.<sup>2</sup> Hence, much research has been directed toward both discovering new materials for supercapacitors and the introduction of new methods to engineer previously known materials.<sup>3</sup> Different types of carbon such as carbon nanotubes, carbon aerogels and activated carbon, as well as

transition metals, such as Ru, Ni, Mn, and their oxides, have been employed as active materials in the fabrication of supercapacitor electrodes.<sup>4–8</sup> However, many of these require the use of toxic chemicals and elaborate procedures, thus limiting the availability of environmentally friendly supercapacitors. Furthermore, the high cost of these materials might render them unfeasible for practical everyday use.<sup>9–11</sup> Thus, there is an urgent need for the development of new inexpensive, light-weight and environmentally friendly energy conversion and storage devices.<sup>12</sup>

The search for alternative high-performance materials has led to a renewed interest in titanium dioxide (TiO<sub>2</sub>)-based supercapacitors. TiO<sub>2</sub> has been considered as one of the most promising materials for widespread applications such as medical implants, photocatalysis, water splitting, photo-electrochromics, hydrogen storage, sensors, solar cells, *etc.*, because of its high chemical stability over a wide range of pH, low cost, biocompatibility, long-term thermodynamic stability and photostability.<sup>13</sup> However, it is worth pointing out that TiO<sub>2</sub> has received much less attention in the construction of supercapacitors.<sup>3</sup> The semiconductor nature of TiO<sub>2</sub> often leads to low electrochemical activity and poor conductivity thereby restricting its applications for the construction of high performance supercapacitors.<sup>14</sup> To date, many approaches, such as hydrogen treatment of TiO<sub>2</sub> nanotubes, phase transformation of TiO<sub>2</sub> nanocrystals, surface coverage of TiO<sub>2</sub> with graphene and with transition metal oxides, have been reported in order to enhance the electrochemical capacitance of

<sup>a</sup>Faculty of Electrical Engineering, University of Ljubljana, SI-1000 Ljubljana, Slovenia

<sup>b</sup>Faculty of Health Sciences, University of Ljubljana, SI-1000 Ljubljana, Slovenia

<sup>c</sup>Department of Chemistry, Ångström Laboratory, Uppsala University, Lägerhyddsvägen 1, 75120 Uppsala, Sweden

<sup>d</sup>Biosensors and Bioelectronics Centre, Department of Physics, Chemistry and Biology (IFM), Linköping University, Sweden. E-mail: ales.iglic@fe.uni-lj.si;

Fax: (+386) 1476 88 50; Tel: (+386) 1476 88 25

<sup>e</sup>Tekidag AB, UCS, Teknikringen 4A, Mjärdevi Science Park, Linköping 583 30,

Sweden. E-mail: ashutosh.tiwari@liu.se; Fax: (+46) 13 137568; Tel: (+46) 13 282395

† Electronic supplementary information (ESI) available: The HRTEM analysis of TiO<sub>2</sub> microbeads, XPS spectra of modified electrodes (Ti 2p and O 1s peaks), total number of surface states vs applied potential (calculated DOS) of modified electrodes, circuit used for EIS data fitting, specific capacitance of FTO/TiO<sub>2</sub>/DA/DNA calculated from Galvanostatic charge–discharge test versus cycle number. See DOI: 10.1039/c5nr02533h

TiO<sub>2</sub>.<sup>15–20</sup> Recently, much attention has been paid to the use of biomolecules to modify semiconductors to improve electrochemical performance. In particular, biomolecules such as chlorophylls, which have efficient absorption ability for solar energy, have been used to develop solar-responsive semiconductor-biomolecular composites for different applications such as photoelectrochemical cells, photocatalytic processes and artificial photosynthesis.<sup>21–23</sup> Of the various kinds of biomolecules considered for charge storage devices, typically the deoxyribonucleic acid (DNA) family has attracted intense interest.<sup>10,24,25</sup> DNA, with its unique stability, topology vs. chemical and physical behaviour, and programmable base length, together with the capability of self-assembly, is an inexpensive, well-characterised, controllable and easily adaptable material.<sup>26–30</sup>

In this study, we improved the electrochemical performance of TiO<sub>2</sub> for use in a capacitor,<sup>31</sup> by designing a new stable and versatile TiO<sub>2</sub>@DNA bionanocomposite electrode using three-dimensional linker-based covalent functionalisation. We attached DNA to mesoporous TiO<sub>2</sub> microbeads, which possess high surface area, crystallinity, low intra-band gap states, interconnectivity of nanocrystals and also faster electronic transport compared to conventional nanoparticles.<sup>32,33</sup> These properties are of special interest for electrochemical devices and greatly facilitate electron transfer and transport. Furthermore, mesoporous TiO<sub>2</sub> microbeads are highly biocompatible.<sup>34</sup> The resulting mesoporous nanohybrids were characterised by scan-

ning electron microscopy (SEM) and transmission electron microscopy (TEM). The surface adsorbates were studied by XPS. The electrochemical properties of the TiO<sub>2</sub>@DNA nanohybrid electrodes were characterised and the role of electrode surface modification on its charge storage, chemical capacitance and trap distribution states was investigated. Finally, the supercapacitor performance of the FTO/TiO<sub>2</sub>/DA/DNA electrode was evaluated using cyclic voltammetric and galvanostatic techniques in PBS buffer as the electrolyte. The overall purpose of this research was to make environmentally friendly electrochemical capacitor electrodes based on a new bionanocomposite material, and to understand the role of DNA in improving the performance of charge storage devices.

## Results and discussion

The morphology of the obtained mesoporous TiO<sub>2</sub> microbeads was characterised by SEM, as shown in Fig. 1a. The size distribution of the TiO<sub>2</sub> microspheres was very uniform (monodisperse) with an average diameter of 500 ± 50 nm, while their surfaces were rough. As can be seen in the selected area electron diffraction (SAED) patterns (Fig. 1b), the TiO<sub>2</sub> microbeads exhibited very high crystallinity in the anatase phase. XRD pattern of the mesoporous TiO<sub>2</sub> microbeads is presented in Fig. 1c. All (101) (004) (200) (105) (211) (213) (204) (220) (215)

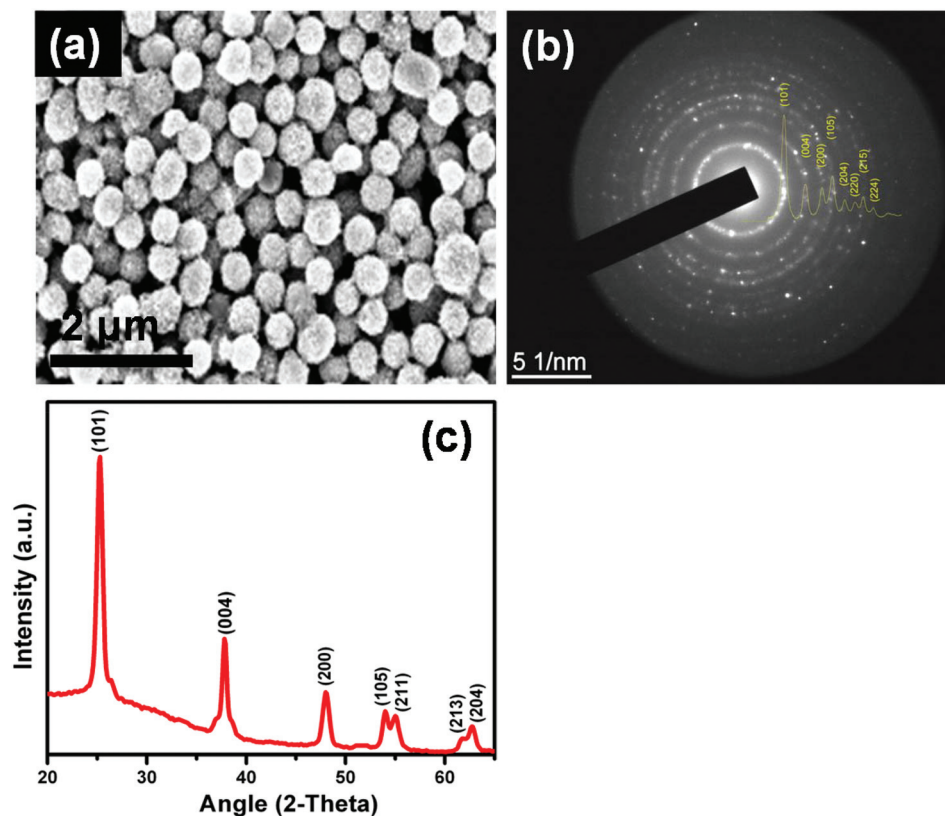


Fig. 1 (a) SEM image, (b) selected area electron diffraction (SAED) patterns and (c) X-ray diffraction patterns of mesoporous TiO<sub>2</sub> microbeads.

(224) planes observed in the XRD and SAED patterns are related to the anatase phase of  $\text{TiO}_2$  (PDF number: 21-1272). The crystallite size was calculated by the Debye–Scherrer formula as 14 nm. The SAED and XRD patterns also showed a pair of strong (101) reflection rings, indicating that the (101) crystal planes of  $\text{TiO}_2$  anatase nanocrystals were locally preferentially oriented.

Fig. 2 presents TEM images of single mesoporous  $\text{TiO}_2$  microbead particles. Fig. 2a shows the uniform contrast of the TEM image from the edge to the centre of a single sphere, indicating that the entire  $\text{TiO}_2$  microbead was composed of self-organised  $\text{TiO}_2$  nanocrystals with a high surface area and porosity. In the high magnification micrographs (Fig. 2b and c) constituent nanocrystals with different shapes were clearly visible and evidently adopted random orientations. Fig. 2d–f show the constituent single nanocrystals ( $15 \pm 5$  nm) of anatase  $\text{TiO}_2$ . A close examination of single  $\text{TiO}_2$  constituent nanocrystals by high resolution TEM (HRTEM) showed that they are completely crystalline along their entire lengths and the clear visibility of crystal lattice fringes. Further HRTEM images of single  $\text{TiO}_2$  nanocrystals with different shapes and distinctively visible lattice fringes are presented in Fig. 3a, with a clearly visible lattice showing a high degree of crystallinity and phase purity. From the distance between the adjacent lattice fringes, the lattice planes on the nanocrystals could be determined (Fig. S1 in ESI†).

The coordination of the surface Ti metal atoms on the small  $\text{TiO}_2$  nanocrystals is incomplete. Thereby they exhibit a

high affinity for oxygen and oxygen-containing ligands.<sup>35</sup> Enediol ligands such as dopamine have a great affinity for these under-coordinated surface Ti sites, restoring the coordination of Ti atoms to an octahedral geometry and forming a ligand-to-metal charge transfer complex.<sup>36,37</sup> Fig. 3b shows the HRTEM image of a mesoporous  $\text{TiO}_2$  microbead coated with a dopamine layer. For comparison, a bare  $\text{TiO}_2$  nanocrystal is also shown (Fig. 3a). In Fig. 3b the amorphous edge on the dopamine coated  $\text{TiO}_2$  nanocrystal can be clearly seen. The thickness of dopamine shell varied from 1 to 3 nm. The HRTEM analysis shows that the exposure of  $\text{TiO}_2$  nanocrystals to dopamine resulted in preferential binding of dopamine to the defect tips of the  $\text{TiO}_2$  nanocrystal surface. This preferential binding was the result of the optimal matching of the enediol groups of dopamine molecules with the uncoordinated titanium atoms found at the nanocrystal on the  $\text{TiO}_2$  surface. The coordination of  $\text{TiO}_2$  surface atoms, and thus the nature of surface defects, is expected to be dependent on the size and shape of the nanocrystals.

Fig. 4 presents XPS spectra of modified electrodes. XPS spectra of C 1s, N 1s and P 2p, principal elements of dopamine and DNA are presented in the Fig. 4a–c. Ti 2p and O 1s peaks, which are characteristic of  $\text{TiO}_2$  are presented in Fig. S2 (in the ESI).† The C 1s spectrum (Fig. 4a) following the adsorption of dopamine on the  $\text{TiO}_2$  surface, can be fitted with two Gaussian peaks at 284.5 and 285.9 eV. The peak at a lower binding energy originates from hydrocarbon groups (C–H, C–C). The peak at a higher binding energy belongs to carbon atoms that

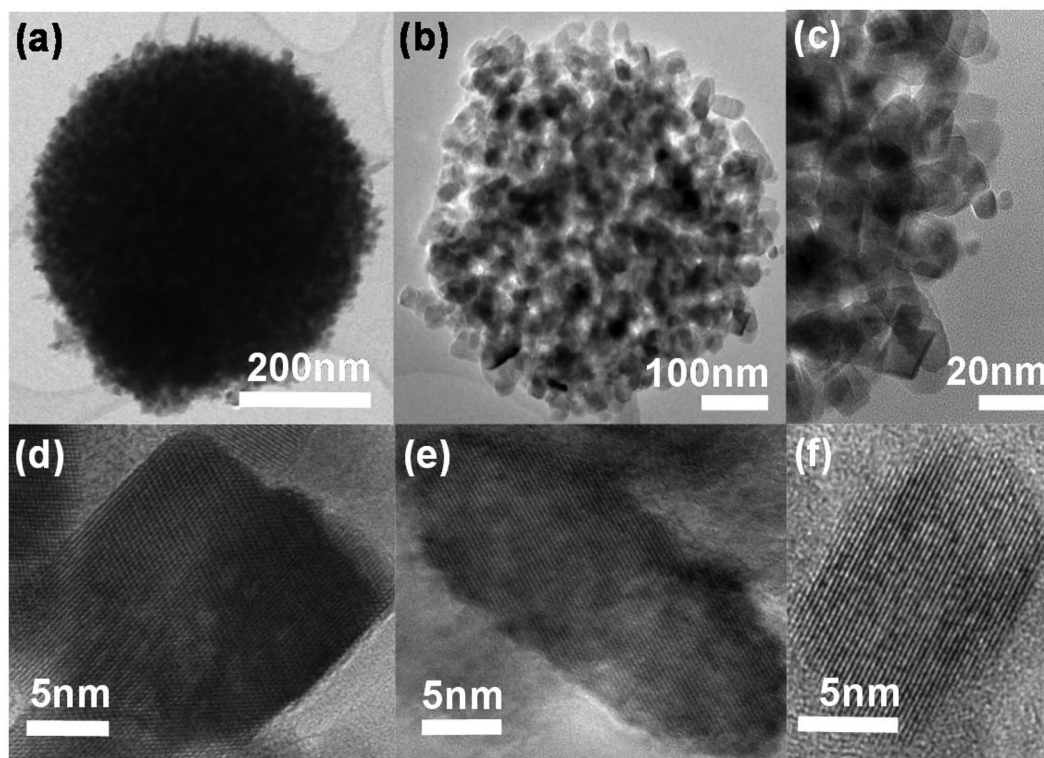
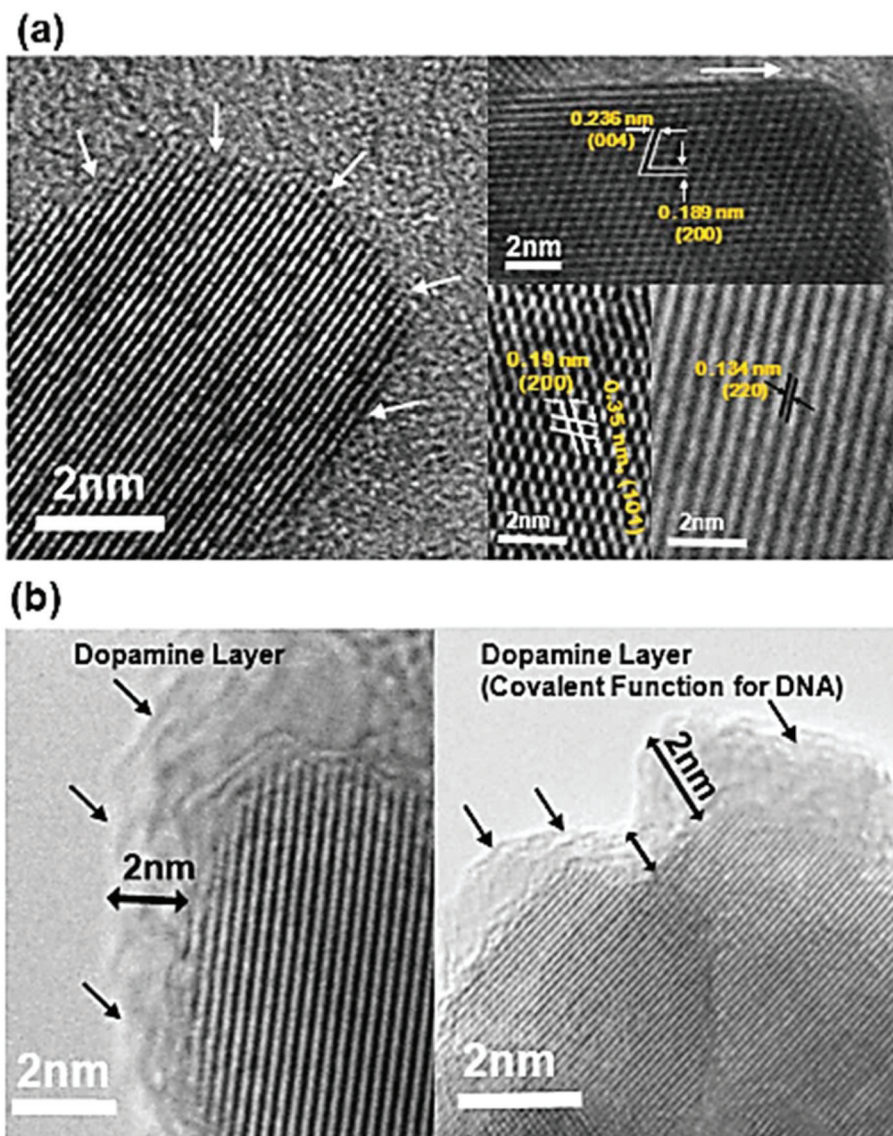


Fig. 2 (a–c) TEM images of a single mesoporous  $\text{TiO}_2$  microbead; (d–f) HRTEM images of constituent single nanocrystals ( $15 \pm 5$  nm) of anatase  $\text{TiO}_2$  microbeads with different sizes and shapes.



**Fig. 3** HRTEM images: (a) bare TiO<sub>2</sub> nanocrystal, selected HRTEM images of constituent nanocrystals. (b) TiO<sub>2</sub> nanocrystal functionalised with dopamine; the amorphous edge on the TiO<sub>2</sub> surface shows a layer of dopamine bonded on the TiO<sub>2</sub> nanocrystals.

are attached to oxygen or nitrogen atoms in the dopamine molecule.<sup>38</sup> In the C 1s spectrum of TiO<sub>2</sub>/DA/DNA the major peaks expected from nucleotide-bases are present; these peaks can be uniquely assigned to the carbon species present in these samples: hydrocarbons (C-C, C-H), carbon bound to nitrogen (C-N, N-C-N), amide carbon (N-C=O) and urea carbon [N-C(=O)-N], with characteristic binding energies of approximately 284, 285, 287 and 288 eV, respectively. Upon conjugation with sugar and phosphate to form nucleosides and nucleotides, additional carbon species are expected to be present in the form of alcohol (C-OH) and cyclic ether (C-O-C) at ~286.5 eV.<sup>39</sup> For the N 1s spectrum of TiO<sub>2</sub>/DA shown in Fig. 4b, the peak at 399.8 eV can be assigned to the NH<sub>2</sub> group of the dopamine molecule. The N 1s spectrum of TiO<sub>2</sub>/DA/DNA is more complicated due to the contributions of different molecular species containing nitrogen atoms. The N 1s XPS

spectra can be divided into two important regions: the region above 400 eV and the region around 398–399 eV. The higher energy peak is attributed to singly-bonded amino N-sites. The peak at the lower binding energy can be attributed to amino groups with a double N=C bond.<sup>40</sup> For the TiO<sub>2</sub>/DA/DNA sample, a single P 2p peak at 133.6 eV is common to all nucleotides (see Fig. 4c). The presence of P- or, to a larger extent, N- and P- together, is an excellent indicator of DNA molecules adsorbed on the TiO<sub>2</sub>/DA surface, their presence being typically unaffected by surface contamination during sample preparation and handling.<sup>41</sup>

Fig. 5a shows cyclic voltammograms of FTO/TiO<sub>2</sub>, FTO/TiO<sub>2</sub>/DA and FTO/TiO<sub>2</sub>/DA/DNA electrodes. The voltammograms of all the electrodes showed the hysteric shape characteristic of electron accumulation/discharge in semiconductor nanocrystalline films.<sup>42</sup> Applying an increasing negative

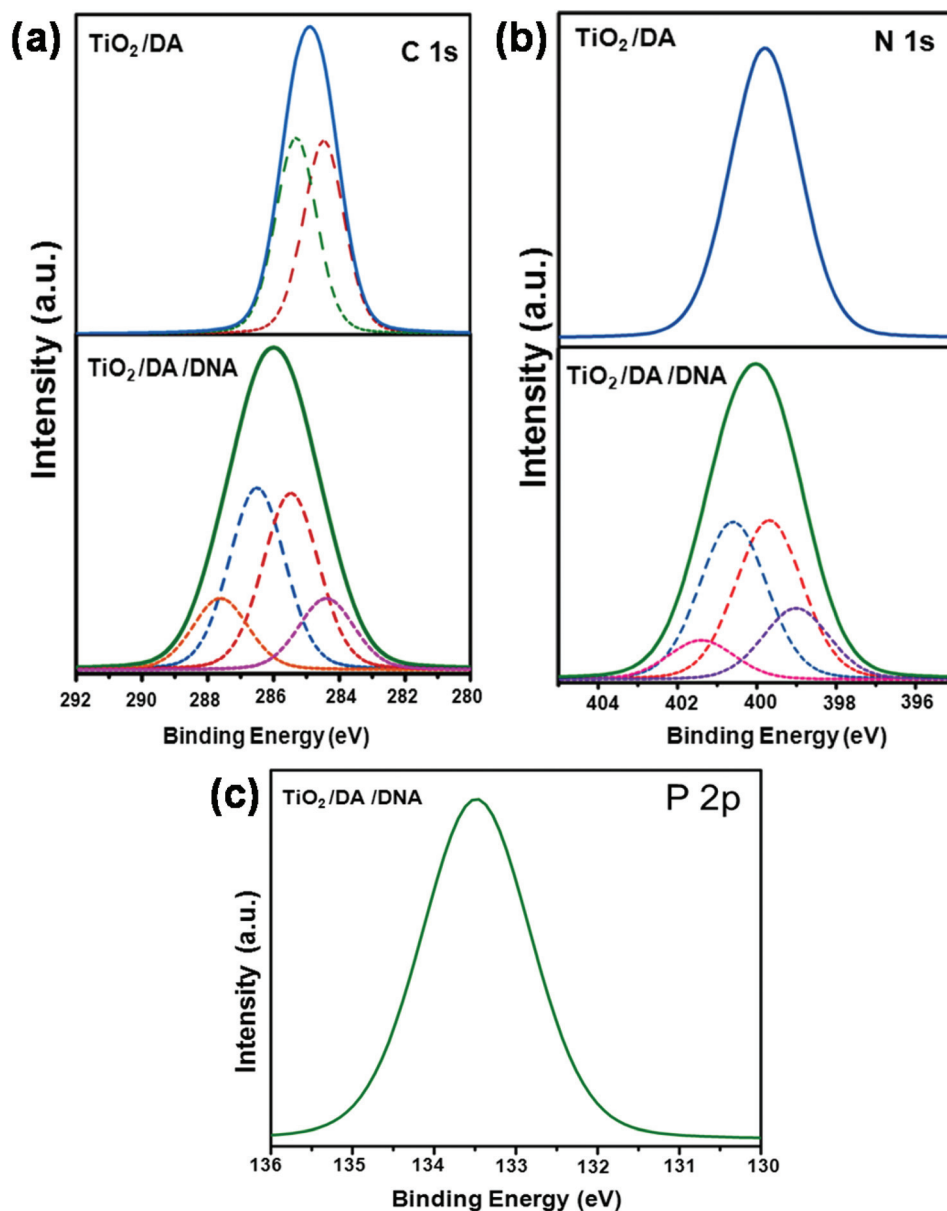


Fig. 4 XPS spectra for the principal elements of the electrodes: experimental data (solid line) and fitting results (dashed line), (a) C 1s, (b) N 1s (c) P 2p common element for DNA.

potential, *i.e.*, a forward bias, to the TiO<sub>2</sub> layer moved the quasi-Fermi level closer toward its conduction band and led to a capacitive current.<sup>43</sup> In principle, for a perfect n-type semiconductor, charge injection should be turned on once the Fermi level reaches the edge of the conduction band.<sup>44</sup> The energetic distribution of acceptor states in the surface of the mesoscopic TiO<sub>2</sub> electrode can be derived directly from the cyclic voltammograms, since the current  $I(V)$  is proportional to the differential capacity ( $C$ ) in a linear sweep (constant scan rate,  $dV/dt = \nu$ ).<sup>45</sup>

$$\frac{dQ}{d\nu} = \text{DOS} \frac{N_A}{F} \quad (1)$$

$$dQ = \frac{1}{\nu} I(V) dV \quad (2)$$

where  $N_A$  is the Avogadro constant,  $F$  is Faraday's constant,  $I(V)$  is the current,  $V$  is the potential applied on the electrode, and  $\nu$  represents the constant scanning rate in the cyclic voltammetry measurements. Dividing  $dQ/dV$  by the elementary charge in eqn (1) yields the density of occupied states (DOS), while integration of eqn (2) gives the total number of surface states ( $Q$ ) which can be plotted as a function of the applied potential, as presented in Fig. S3.<sup>†</sup> As shown in Fig. S3,<sup>†</sup> the onset of the voltammogram of TiO<sub>2</sub>/DA/DNA shifted positively (50 mV) due to surface protonation by the carboxylic acid group.<sup>47</sup> Fig. 5a indicates that the current from the FTO/TiO<sub>2</sub>/DA/DNA elec-

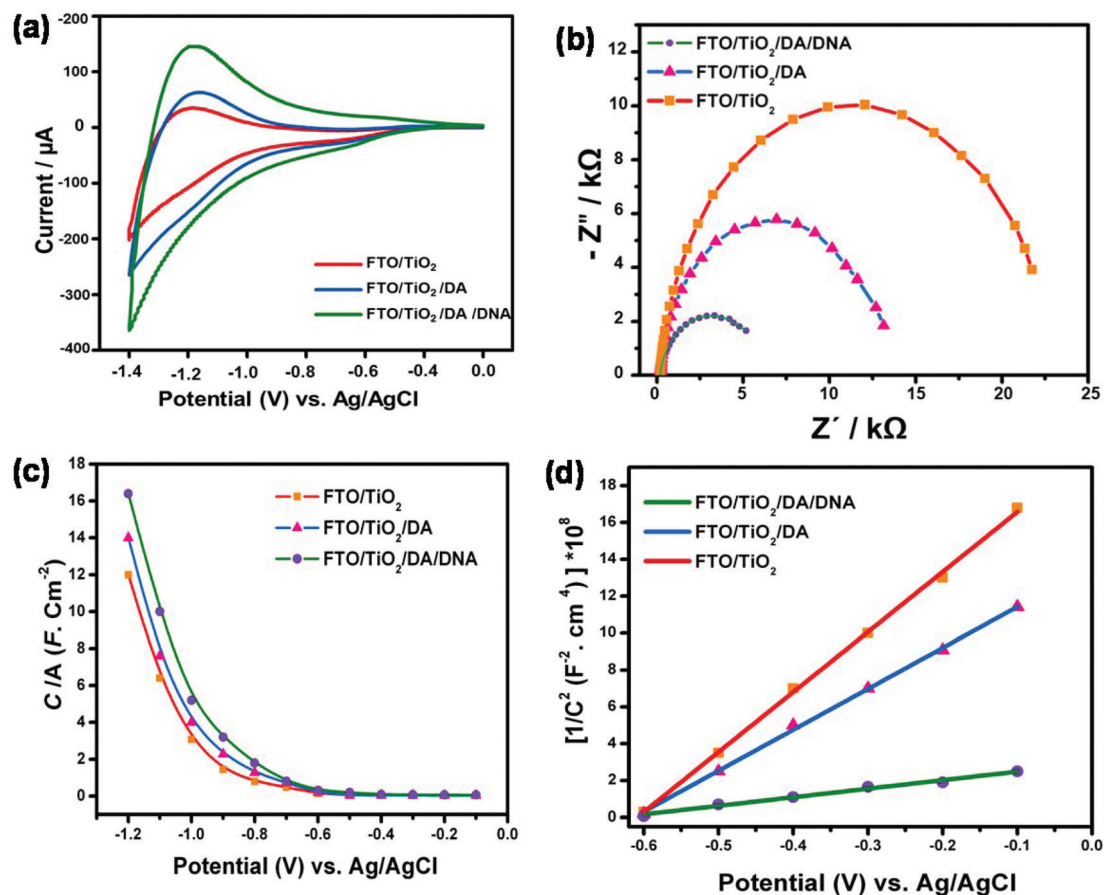


Fig. 5 Electrochemical characterisation of different modified electrodes: FTO/TiO<sub>2</sub>, FTO/TiO<sub>2</sub>/DA, FTO/TiO<sub>2</sub>/DA/DNA in PBS; (a) cyclic voltammetry, (b) EIS spectra with dc potential of  $-0.6$  V, (c) capacitance obtained from EIS measurement *via* applied potential, (d) Mott–Schottky plots.

trode and therefore the DOS increased significantly relative to the value measured for FTO/TiO<sub>2</sub>. The amount of charge stored in the bare TiO<sub>2</sub> and TiO<sub>2</sub> coated with dopamine and DNA molecular layers was calculated from the current determined in the CV measurements. In the case of a bare FTO/TiO<sub>2</sub>, the amount of stored charge was found to be  $\sim 1$  mC, while the charge stored in the FTO/TiO<sub>2</sub>/DA and FTO/TiO<sub>2</sub>/DA/DNA electrodes was calculated to be  $\sim 1.5$  mC and 3 mC, respectively. This result indicates that the charge storage capacity of TiO<sub>2</sub>/DA/DNA increased compared to the FTO/TiO<sub>2</sub> electrode, indicating the potentially important role of DNA for enhancement of charge storage capacity of TiO<sub>2</sub> in the fabrication of powerful charge storage devices.

The high electric current in the FTO/TiO<sub>2</sub>/DA/DNA electrode indicates an efficient charge transport from TiO<sub>2</sub> to DNA. Presumably, this result was the consequence of the coupling of dopamine and DNA with the TiO<sub>2</sub> microbead surface to form a bio-hybrid, so that the energy levels are mixed, which favours the possibility of a higher energy transfer. This phenomenon resulted from the donor–bridge–acceptor system with electron transfer across the biomolecule–nanostructure interface.<sup>48</sup> The reduction of DNA molecules grafted on a mesoscopic TiO<sub>2</sub> film can be carried out by electrons that are injected from the FTO

glass electrode into the semiconductor particles and migrate in the conduction band of the semiconductor *via* interfacial charge transfer.<sup>49</sup> This involves direct transfer from the conduction band, and also intermediate trapping at surface states, with further charge transfer from the surface states to the isoenergetic DNA acceptor levels or *via* surface states to be finally transferred to the DNA acceptor.<sup>50</sup> This implies an electron flow either in the conduction band of the semiconductor or in the trap states along its surface.<sup>51</sup>

To acquire complementary information on the different processes contributing to the result obtained from the CV measurements, we studied the electrochemical impedance spectra of the different electrodes in the range of potentials in which the CVs were measured, using methods of interpretation of impedance that have already been described.<sup>52</sup> Fig. 5b shows typical electrochemical impedance spectra (EIS) of modified electrodes at  $-0.6$  V. At the more negative potentials, here beyond  $-0.6$  V, at which the TiO<sub>2</sub> network is conducting, the EIS data were well fitted by the simple circuit as shown in Fig. S4.† At these negative potentials, electron transport resistance becomes negligible and the capacitance of the high-surface-area TiO<sub>2</sub> is much larger than that of the FTO. Fitting the low-frequency semicircle subsequently gives the chemical

capacitance ( $C_{\mu}$ ) and charge transfer resistance ( $R_{ct}$ ).<sup>53</sup> The charge transfer resistance is essentially controlled by the surface modification of the TiO<sub>2</sub> mesoporous films (Fig. 5b). A significant difference in the  $R_{ct}$  values was observed upon the step-wise formation of the modified electrode. The  $R_{ct}$  decreased sharply from 22 kΩ for FTO/TiO<sub>2</sub> to 13 kΩ for FTO/TiO<sub>2</sub>/DA and to 5 kΩ for FTO/TiO<sub>2</sub>/DA/DNA. The results show a higher electron transfer rate from the DNA conjugated electrode to the Na<sup>+</sup> cations of the electrolyte solution. The ssDNA arm has a charged backbone that can bind to various metal ions and support ionic conductivity.<sup>54</sup>

The chemical capacitance is proportional to the electron density ( $n$ ) at a given position of the Fermi level, which depends on the potential  $V = (E_{Fn} - E_{F0})/e$ . It has been shown that the electron density depends exponentially on the Fermi level:

$$n = n_0 \exp[\alpha(E_{Fn} - E_{F0})]/k_B T \quad (3)$$

where  $n_0$  is the equilibrium value of the electron concentration,  $k_B$  is the Boltzmann constant,  $T$  is the temperature,  $\alpha$  is a coefficient describing either the Boltzmann occupancy of the conduction band capacitance ( $\alpha = 1$ ) or an exponential distribution of trap states ( $\alpha < 1$ ).<sup>55</sup>

The calculated values of  $C_{\mu}$  for different electrodes at different applied biases (different Fermi levels) are plotted in Fig. 5c. It can be seen in Fig. 5c that the capacitance of the electrode increased with surface modification. The exponential behaviour of the electrodes was in good agreement with the proposed model,<sup>56</sup> which represents two main regions.<sup>57</sup> The first one at very low cathodic potentials is dominated by a low capacitance, which follows the Mott-Schottky behaviour; the second is at high cathodic potentials, where the capacitance changes from Mott-Schottky behaviour to an exponential rise with increasing forward bias.<sup>58</sup>

Fig. 5d represents the Mott-Schottky plots of the observed capacitance for all electrodes. Carrier density can be quantified from the slope of Mott-Schottky analysis by using the equation<sup>59</sup>:

$$\left(\frac{A}{C}\right)^2 = \frac{2}{e\epsilon_0\epsilon N_D} \left(V - E_{fb} - \frac{k_B T}{q}\right) \quad (4)$$

where  $C$  is the capacitance,  $\epsilon$  is the dielectric constant of the semiconductor,  $\epsilon_0$  is the permittivity of free space ( $8.854 \times 10^{-12} \text{ C V}^{-1} \text{ m}^{-1}$ ),  $A$  is the area of the electrode,  $e$  is the elementary charge,  $N_D$  is the donor concentration,  $V$  is the applied potential, and  $E_{fb}$  is the position of the flat band potential.

As shown in Mott-Schottky plots (Fig. 5d), all electrodes (FTO/TiO<sub>2</sub>, FTO/TiO<sub>2</sub>/DA, FTO/TiO<sub>2</sub>/DA/DNA) exhibit positive slopes as expected for n-type semiconductors. Apparently, the FTO/TiO<sub>2</sub>/DA, FTO/TiO<sub>2</sub>/DA/DNA electrodes exhibit a similar slope of the Mott-Schottky plot with the FTO/TiO<sub>2</sub>. With an  $\epsilon$  value of 170 for TiO<sub>2</sub>, electron densities of TiO<sub>2</sub>, TiO<sub>2</sub>/DA and TiO<sub>2</sub>/DA/DNA electrodes were calculated to be  $2.5 \times 10^{20} \text{ cm}^{-3}$ ,  $3.8 \times 10^{20} \text{ cm}^{-3}$  and  $18 \times 10^{20} \text{ cm}^{-3}$ , respectively. Our experimental results (Fig. 5c and d) show that the chemical capaci-

tance and donor densities of the TiO<sub>2</sub> porous network increased with surface modification. The donor density plays a key role in determining electronic conductivity; increasing of donor density by surface modification leads to improvement of conductivity and charge storage ability of an electrode.<sup>60</sup> The induction of new surface states (*via* surface modification) and also charge transfer from n-type TiO<sub>2</sub> to p-type DNA, are responsible for the observed changes in the charge capacitance. According to the Marcus theory, proper electronic coupling of donor-acceptor energy states can facilitate this charge transfer. When the donor and the acceptor states are sufficiently close, quantum-mechanical tunnelling can occur, through the bridging of the molecular medium between the donor and the acceptor sites.<sup>61</sup>

### Electrochemical supercapacitor study of TiO<sub>2</sub>@DNA nano-hybrids

Fig. 6a shows a comparison of the overlaid CVs of the FTO/TiO<sub>2</sub>, FTO/TiO<sub>2</sub>/DA, FTO/TiO<sub>2</sub>/DA/DNA electrodes at a scan rate of 500 mV s<sup>-1</sup> in PBS. The three electrodes produced near rectangular shaped plots, which illustrate the near ideal capacitive behaviour of the electrodes. Further, the FTO/TiO<sub>2</sub>/DA/DNA electrode displayed a higher integrated area compared to the FTO/TiO<sub>2</sub>, FTO/TiO<sub>2</sub>/DA electrode, confirming the enhancement of the electrochemical capacitance of TiO<sub>2</sub> by addition of DNA.

Cyclic voltammograms (CV) measured at different voltage scan rates for FTO/TiO<sub>2</sub>/DA/DNA are shown in Fig. 6b. All the CV plots are close to rectangular in shape representing the near ideal capacitive properties of working electrodes. The relationship between the specific capacitance and scan rates is shown in Fig. 6c. The decrease in the specific capacitance with increasing scan rate is due to the ineffective ion accumulation on porous electrodes at high scan rates. From Fig. 6c it can be observed that the FTO/TiO<sub>2</sub>/DA/DNA exhibited higher specific capacitance compared to both FTO/TiO<sub>2</sub> and FTO/TiO<sub>2</sub>/DA electrodes at all scan rates. The maximum specific capacitance of the FTO/TiO<sub>2</sub>, FTO/TiO<sub>2</sub>/DA, FTO/TiO<sub>2</sub>/DA/DNA electrodes was 5 and 5.4 F g<sup>-1</sup> and 8 F g<sup>-1</sup>, respectively, at a scan rate of 5 mV s<sup>-1</sup>.

The near ideal capacitive behaviour of the as-prepared electrodes could be further confirmed by galvanostatic charge-discharge. Fig. 7a presents the galvanostatic curves of FTO/TiO<sub>2</sub>/DA/DNA at different current densities. It can be seen that all curves exhibit a nearly symmetrical triangular shape, suggesting the good electrochemical behaviour of the electrode. The dramatic decrease in the specific capacitance as a function of the current density increase can also be explained by the inefficiency of ion accumulation.

The specific capacitance of the FTO/TiO<sub>2</sub>/DA/DNA at a current density of 0.6 A g<sup>-1</sup> is presented in Fig. S5.† From the galvanostatic result it is evident that even after 1200 cycles, fairly stable capacitance is maintained, and no change in charge-discharge can be observed. At the end of hundred cycles, the FTO/TiO<sub>2</sub>/DA/DNA electrode maintains a symmetric

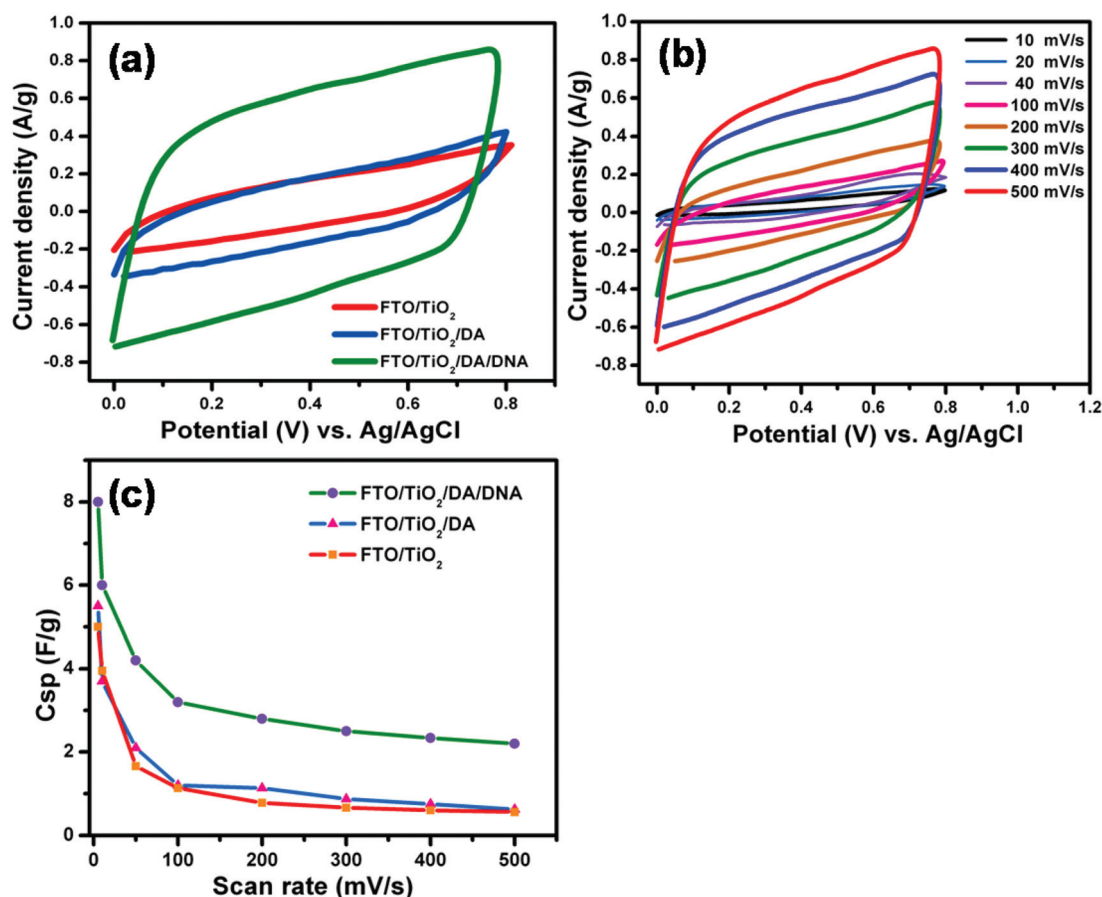


Fig. 6 Electrochemical performance of a modified electrode in PBS solution. (a) cyclic voltammetry of FTO/TiO<sub>2</sub>, FTO/TiO<sub>2</sub>/DA, FTO/TiO<sub>2</sub>/DA/DNA at scan rate of 500 mV s<sup>-1</sup>, (b) cyclic voltammetry of FTO/TiO<sub>2</sub>/DA/DNA at different scan rate of (5–500 mV s<sup>-1</sup>), (c) specific capacitances as a function of the scan rates obtained from the CV data of FTO/TiO<sub>2</sub>, FTO/TiO<sub>2</sub>/DA, FTO/TiO<sub>2</sub>/DA/DNA electrodes.

charge–discharge shape with approximately 97% capacitance retention.

The long-term cycling stability of the FTO/TiO<sub>2</sub>/DA/DNA electrode was further evaluated by repeating the CV measurement at a scan rate of 50 mV s<sup>-1</sup> for 1500 cycles. From Fig. 7b, it can be seen that the capacitance only decreases by about 5% of the initial capacitance, even after 1500 cycles, indicating a good cycling life of the electrode materials. This excellent cycling stability in most biofluids (PBS) is the pivotal advantage of our device as an energy storage device in bioenvironments, because we can design supercapacitors as power-supply for medical implanted devices which can directly utilise physiological fluids as a source of electrolyte. Such devices could potentially be implanted inside fluid rich organs such as blood vessels, the eye or bladder without cumbersome packages.<sup>10</sup>

## Experimental

### Materials

Dopamine hydrochloride (DA, 99.99%) was purchased from Sigma-Aldrich, Germany and a single-stranded oligodeoxyribo-

nucleotide (ss-OGN) was purchased from Eurofins MWG Operon, Germany with a 5'-terminal carboxyl group (HPLC grade, 50mer, 5'-GGGCCTGGTCTACCAAGCAAACCTCCAG-TACGCCAGGGAACATGAGAGGG) and kept as a 10 μM solution in phosphate buffer at pH 7.4.

### Preparation of TiO<sub>2</sub>@DNA nanohybrids

Biocompatible mesoporous TiO<sub>2</sub> microbeads were synthesised by the solvothermal method as we reported previously.<sup>20</sup> A paste consisting of mesoporous TiO<sub>2</sub> microbeads and ethyl cellulose in terpineol was deposited using the doctor blade technique on fluorine-doped tin oxide conducting glass (FTO, TEC15, Hartford Glass) to form a transparent layer.<sup>57</sup> After drying in air, the electrodes were sintered at 500 °C for 30 minutes. The thickness of the fabricated mesoporous TiO<sub>2</sub> microbead film was measured using a Dektak profilometer (VEECO/SLOAN DEKTAK 3, New York, US) as 4 μm following the first step and the electrode was denoted as FTO/TiO<sub>2</sub>. The TiO<sub>2</sub> modified electrode was rinsed carefully in deionised water and then dipped into a freshly prepared 10 mM aqueous dopamine solution. The dopamine covered electrode was then rinsed carefully several times with deionised water to remove

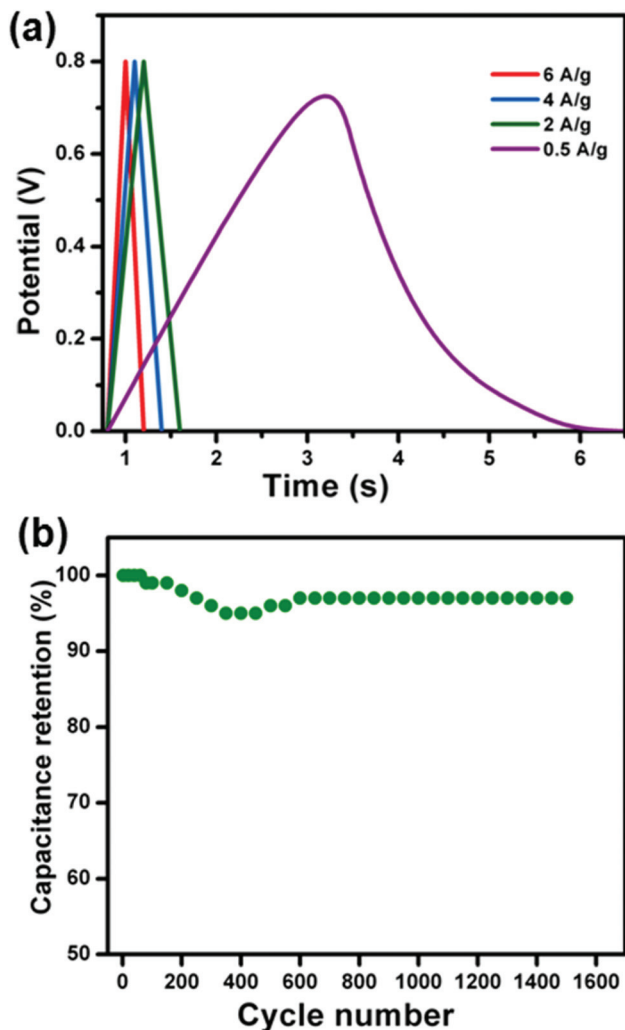


Fig. 7 (a) Galvanostatic charge–discharge curves at different current densities ( $0.5 \text{ A g}^{-1}$ ,  $6 \text{ A g}^{-1}$ , and (b) cyclic stabilities; of FTO/TiO<sub>2</sub>/DA/DNA in the PBS.

excess non-chemisorbed dopamine from the surface. In this step, the electrode was denoted as FTO/TiO<sub>2</sub>/DA. A condensation reaction through the intermediate *N*-hydroxy succinimide ester was used to bind the carboxyl group of the oligonucleotide to the amino group of dopamine by an amide bond. In the final step, the FTO/TiO<sub>2</sub>/DA modified electrode was immersed in DNA solution ( $10 \mu\text{M}$  in phosphate buffer of pH 7.4) overnight at  $4 \text{ }^\circ\text{C}$  for DNA adsorption. The electrodes were then washed with deionised water, dried at room temperature, and were then ready for use. Following the last step, the electrode was denoted as FTO/TiO<sub>2</sub>/DA/DNA.

### Characterisation

The mesoporous TiO<sub>2</sub> microbead particle morphology was examined with a Hitachi S4700 field-emission scanning electron microscope (SEM, Hitachi, Tokyo, Japan). Transmission electron microscopy (TEM) and selected-area electron diffrac-

tion (SAED), using a Jeol JEM-2100 (JEOL, Tokyo, Japan), operating at 200 kV, were used for the determination of the overall shape and appearance of the mesoporous TiO<sub>2</sub> microbead and for detecting the dopamine shell formed on the mesoporous TiO<sub>2</sub> microbead. The SAED measurements were performed on a cluster of 0.9 nm particles. The crystal structure properties of the mesoporous TiO<sub>2</sub> microbead were obtained by hard X-ray low-angle reflectivity measurements, using the Philips PW1710 powder diffractometer (Philips, Amsterdam, Netherlands) with a copper anode source Cu-K alpha,  $\lambda = 1.54 \text{ \AA}$ , operating at 0.8 kW and with an accuracy of  $0.015^\circ$  2theta. The intensity was detected with a proportional Xe-gas filled detector. The X-ray photoelectron spectroscopy (XPS) analyses were carried out on a PHI-TFA XPS spectrometer produced by Physical Electronics Inc. The sample was introduced into a ultra-high vacuum chamber. The analysed area was 0.4 mm in diameter and about 3–5 nm in depth. This high surface sensitivity is a general characteristic of the XPS method. Sample surfaces were excited by X-ray radiation from a monochromatic Al source at a photon energy of 1486.6 eV. The high-energy resolution spectra were acquired with an energy analyser operating at a resolution of about 0.6 eV and a pass energy of 29 eV. For the calibration of the measured data, the spectra from the surface were aligned by setting the C 1s peak, characteristic of C–C bonds, at 285.0 eV. The accuracy of the binding energies obtained was about  $\pm 0.3 \text{ eV}$ . The peaks in the elemental core-level spectra were fitted using CasaXPS commercial XPS analysis software. The number of peaks chosen for each fit was the minimal number required to obtain random residuals. A convolution of Lorentzian and Gaussian line shapes was used to fit the individual peaks. A linear combination of Shirley and linear functions was used to model the background, with the corresponding coefficients fitted simultaneously with the peaks.

### Electrochemical characterisation

Electrochemical measurements were carried out in a conventional three-electrode system using a modified FTO (FTO/TiO<sub>2</sub>, FTO/TiO<sub>2</sub>/DA, FTO/TiO<sub>2</sub>/DA/DNA) electrode as the working electrode, a platinum wire as the counter electrode, and a Ag/AgCl (3 M KCl) reference electrode. The electrochemical signals were recorded in a phosphate buffer solution at pH 7.4 using IviumStat (Ivium, Netherlands). Cyclic Voltammetry (CV) was recorded at a scan rate of  $50 \text{ mV s}^{-1}$ , each sample measurement being repeated for 50 cycles. The amplitude of the ac signal used for electrochemical impedance spectroscopy measurements was 10 mV, and the frequency ranged between 10 kHz and 10 mHz. For the three electrodes mentioned above, the electrochemical impedance spectroscopy measurements were performed under a dc potential ranging between  $-0.1$  and  $-0.6 \text{ V}$ . All potentials are reported against the Ag/AgCl reference electrode.

### Supercapacitor measurement

Cyclic voltammetry and galvanostatic charge–discharge curves were measured using IviumStat (Ivium, Netherlands). During

the CV measurements, a potential range of 0.0 to 0.8 V was applied with a voltage sweep rate of 5–500 mV s<sup>-1</sup>. The specific capacitances of the as-fabricated electrodes were calculated from the CV curves, according to the following equation:

$$C_s = \frac{\int Id\nu}{m\nu\Delta V}$$

where  $C_s$  is the specific capacitance (F g<sup>-1</sup>),  $m$  is the mass of the active material (g),  $\nu$  is the scan rate (mV s<sup>-1</sup>),  $\Delta V$  is the potential window (V) and  $\int Id\nu$  is the integrated area of the CV curve.

The specific capacitance of the as-fabricated electrodes was calculated from the charge–discharge data according to the following equation:

$$C_s = \frac{I\Delta t}{\Delta V m}$$

where  $C_s$  is the specific capacitance,  $I$  is the constant discharging current,  $\Delta t$  is the discharging time,  $\Delta V$  is the potential window, and  $m$  is the mass loading of the electro-active material.

## Conclusions

We have fabricated TiO<sub>2</sub>@DNA nanohybrid electrodes. XPS analysis confirmed robust binding of DNA to the surface of the electrode. Electrochemical characterisation showed the effect of surface modification on donor density, charge transfer resistance and chemical capacitance, and confirmed the improvement in performance brought about by DNA surface functionalisation of mesoporous TiO<sub>2</sub> microbeads. Donor densities were clearly increased after DNA addition to electrode and reached their highest value of  $18 \times 10^{20}$  cm<sup>-3</sup> for the FTO/TiO<sub>2</sub>/DA/DNA electrode. Charge transfer resistance decreased sharply from 22 k $\Omega$  for FTO/TiO<sub>2</sub> to 13 k $\Omega$  for FTO/TiO<sub>2</sub>/DA and to 5 k $\Omega$  for FTO/TiO<sub>2</sub>/DA/DNA, which indicated that the charge transfer resistance is essentially controlled by the surface modification of the TiO<sub>2</sub> mesoporous film at the applied negative potentials. At a constant Fermi level of -1.2 V versus NHE level, the maximum chemical capacitance value (16.4 mF cm<sup>-2</sup>) was derived after DNA functionalisation of the electrode. Further, the electrode exhibited an excellent cycle life in PBS with a capacitance retention of about 95% after 1500 cycles. These findings could open up new opportunities for nontoxic bionanocomposite materials to construct high-performance supercapacitors as power supplies for medically implantable devices which could operate under *in vivo* conditions. Since the DNA sequence strongly influences DNA conductivity,<sup>62</sup> further work might be targeted on using DNA with different sequences in order to improve the conductivity and supercapacitor performance of nano-biohybrids.

## Acknowledgements

The authors would like to acknowledge the Swedish Research Council (VR- 2011-6058357), R.I. and A.I., Slovenian Research

Agency (ARRS, grants J3-6728, J1-4109, J1-4136, J3-4108 & P2-0232) for generous financial support to carry out this research.

## Notes and references

- 1 M. Winter and R. J. Brodd, *Chem. Rev.*, 2004, **104**, 4245–4270.
- 2 Y. G. Majid Beidaghi, *Energy Environ. Sci.*, 2014, **7**, 867–884.
- 3 G. Wang, L. Zhang and J. Zhang, *Chem. Soc. Rev.*, 2012, **41**, 797–828.
- 4 N. Bagheri, A. Aghaei, M. Y. Ghotbi, E. Marzbanrad, N. Vlachopoulos, L. Häggman, M. Wang, G. Boschloo, A. Hagfeldt, M. Skunik-Nuckowska and P. J. Kulesza, *Electrochim. Acta*, 2014, **143**, 390–397.
- 5 Z. Xu, Z. Li, C. M. B. Holt, X. Tan, H. Wang, B. S. Amirkhiz, T. Stephenson and D. Mitlin, *J. Phys. Chem. Lett.*, 2012, **3**, 2928–2933.
- 6 W. Liu, X. Yan, J. Chen, Y. Feng and Q. Xue, *Nanoscale*, 2013, **5**, 6053–6062.
- 7 M. Kim and J. Kim, *Phys. Chem. Chem. Phys.*, 2014, **16**, 11323–11336.
- 8 M. Zhi, C. Xiang, J. Li, M. Li and N. Wu, *Nanoscale*, 2012, **5**, 72–88.
- 9 J. Hur, K. Im, S. Hwang, B. Choi, S. Kim, S. Hwang, N. Park and K. Kim, *Sci. Rep.*, 2013, **3**, 1–7.
- 10 L. Nyholm, G. Nyström, A. Mihranyan and M. Strømme, *Adv. Mater.*, 2011, **23**, 3751–3769.
- 11 S. Makino, T. Ban and W. Sugimoto, *J. Electrochem. Soc.*, 2015, **162**, A5001–A5006.
- 12 A. S. Aricò, P. Bruce, B. Scrosati, J.-M. Tarascon and W. van Schalkwijk, *Nat. Mater.*, 2005, **4**, 366–377.
- 13 J. Tian, Z. Zhao, A. Kumar, R. I. Boughton and H. Liu, *Chem. Soc. Rev.*, 2014, **43**, 6920–6937.
- 14 M. Salari, S. H. Aboutalebi, A. T. Chidembo, I. P. Nevirkovets, K. Konstantinov and H. K. Liu, *Phys. Chem. Chem. Phys.*, 2012, **14**, 4770–4779.
- 15 G. Zhang, C. Huang, L. Zhou, L. Ye, W. Li and H. Huang, *Nanoscale*, 2011, **3**, 4174–4181.
- 16 X. Lu, M. Yu, G. Wang, T. Zhai, S. Xie, Y. Ling, Y. Tong and Y. Li, *Adv. Mater.*, 2013, **25**, 267–272.
- 17 Z. Zhang, F. Xiao, Y. Guo, S. Wang and Y. Liu, *ACS Appl. Mater. Interfaces*, 2013, **5**, 2227–2233.
- 18 F. Fabregat-Santiago, E. M. Barea, J. Bisquert, G. K. Mor, K. Shankar and C. a Grimes, *J. Am. Chem. Soc.*, 2008, **130**, 11312–11316.
- 19 W. Zhou, X. Liu, Y. Sang, Z. Zhao, K. Zhou, H. Liu and S. Chen, *ACS Appl. Mater. Interfaces*, 2014, **6**, 4578–4586.
- 20 X. Lu, G. Wang, T. Zhai, M. Yu, J. Gan, Y. Tong and Y. Li, *Nano Lett.*, 2012, **12**, 1690–1696.
- 21 A. Mershin, K. Matsumoto, L. Kaiser, D. Yu, M. Vaughn, M. K. Nazeeruddin, B. D. Bruce, M. Graetzel and S. Zhang, *Sci. Rep.*, 2012, **2**, 1–7.
- 22 C. Li, F. Wang and J. C. Yu, *Energy Environ. Sci.*, 2011, **4**, 100–113.

- 23 S. D. Glover, C. Jorge, L. Liang, K. G. Valentine, L. Hammarström and C. Tommos, *J. Am. Chem. Soc.*, 2014, **136**, 14039–14051.
- 24 U. Nithiyantham, A. Ramadoss, S. R. Ede and S. Kundu, *Nanoscale*, 2014, **6**, 8010–8023.
- 25 J. Hur, K. Im, S. W. Kim, U. J. Kim, J. Lee, S. Hwang, J. Song, S. Kim, S. Hwang and N. Park, *J. Mater. Chem. A*, 2013, **1**, 14460–14466.
- 26 V. Bhalla, R. P. Bajpai and L. M. Bharadwaj, *EMBO Rep.*, 2003, **4**, 442–445.
- 27 A. J. Steckl, H. Spaeth, H. You, E. Gomez and J. Grote, *Opt. Photonics News*, 2011, **22**, 34–39.
- 28 A. J. Steckl, *Nat. Photonics*, 2007, **1**, 3–5.
- 29 A. V. Pinheiro, D. Han, W. M. Shih and H. Yan, *Nat. Nanotechnol.*, 2011, **6**, 763–772.
- 30 J. R. Heath and M. a. Ratner, *Phys. Today*, 2003, **56**, 43–49.
- 31 C. Sanchez, B. Julián, P. Belleville and M. Popall, *J. Mater. Chem.*, 2005, **15**, 3559–3592.
- 32 M. Pazoki, N. Taghavinia, A. Hagfeldt and G. Boschloo, *J. Phys. Chem. B*, 2014, **118**, 16472–16478.
- 33 M. Pazoki, J. Oscarsson, L. Yang, B. Park, E. M. J. Johansson, H. Rensmo, A. Hagfeldt and G. Boschloo, *RSC Adv.*, 2014, **4**, 50295–50300.
- 34 R. Imani, P. Veranic, A. Iglic, M. Erdani Kreft, M. Pazoki and S. Hudoklin, *Photochem. Photobiol. Sci.*, 2011, **10**, 135–144.
- 35 B. Geiseler and L. Fruk, *J. Mater. Chem.*, 2012, **22**, 735–741.
- 36 E. A. Rozhkova, I. Ulasov, B. Lai, N. M. Dimitrijevic, M. S. Lesniak and T. Rajh, *Nano Lett.*, 2009, **9**, 3337–3342.
- 37 T. Rajh, J. M. Nedeljkovic, L. X. Chen, O. Poluektov and M. C. Thurnauer, *J. Phys. Chem. B*, 1999, **103**, 3515–3519.
- 38 K. Syres, A. Thomas, F. Bondino, M. Malvestuto and M. Grätzel, *Langmuir*, 2010, **26**, 14548–14555.
- 39 C.-Y. Lee, P. Gong, G. M. Harbers, D. W. Grainger, D. G. Castner and L. J. Gamble, *Anal. Chem.*, 2006, **78**, 3316–3325.
- 40 Y. Zubavichus, O. Fuchs, L. Weinhardt, C. Heske, E. Umbach, J. D. Denlinger, M. Grunze and D. Denlinger, *Radiat. Res.*, 2004, **161**, 346–358.
- 41 D. Y. Petrovykh, H. Kimura-Suda, L. J. Whitman and M. J. Tarlov, *J. Am. Chem. Soc.*, 2003, **125**, 5219–5226.
- 42 F. Fabregat-santiago, I. Mora-sero, G. Garcia-Belmonte and J. Bisquert, *J. Phys. Chem. B*, 2003, **107**, 758–768.
- 43 M. Jankulovska, T. Berger, S. S. Wong, R. Gómez and T. Lana-Villarreal, *ChemPhysChem*, 2012, **13**, 3008–3017.
- 44 I. Mora-sero and J. Bisquert, *Nano Lett.*, 2003, **3**, 945–949.
- 45 I. Abayev, A. Zaban, V. G. Kytin, A. a. Danilin, G. Garcia-Belmonte and J. Bisquert, *J. Solid State Electrochem.*, 2007, **11**, 647–653.
- 46 J. Bisquert, *Phys. Chem. Chem. Phys.*, 2003, **5**, 5360–5364.
- 47 M. Vega-Arroyo, P. R. LeBreton, P. Zapol, L. a. Curtiss and T. Rajh, *Chem. Phys.*, 2007, **339**, 164–172.
- 48 J. van de Lagemaat and A. J. Frank, *J. Phys. Chem. B*, 2000, **104**, 4292–4294.
- 49 J. Bisquert, A. Zaban, M. Greenshtein and I. Mora-Seró, *J. Am. Chem. Soc.*, 2004, **126**, 13550–13559.
- 50 T. Lee, A. K. Yagati, J. Min and J.-W. Choi, *Adv. Funct. Mater.*, 2014, **24**, 1781–1789.
- 51 R. L. Mccreery, *Chem. Mater.*, 2004, **16**, 4477–4496.
- 52 J. Bisquert, G. Garcia-Belmonte, F. Fabregat-santiago, S. Ferriols, P. Bogdanoff and E. C. Pereira, *J. Phys. Chem. B*, 2000, **104**, 2287–2298.
- 53 J. Bisquert, *Phys. Rev. B: Condens. Matter*, 2008, **77**, 235203–235215.
- 54 Q. Wang, S. Ito, M. Grätzel, F. Fabregat-Santiago, I. Mora-Seró, J. Bisquert, T. Bessho and H. Imai, *J. Phys. Chem. B*, 2006, **110**, 25210–25221.
- 55 J. Garcia-Cañadas, F. Fabregat-Santiago, J. Kapla, J. Bisquert, G. Garcia-Belmonte, I. Mora-Seró and M. O. M. Edwards, *Electrochim. Acta*, 2004, **49**, 745–752.
- 56 F. Fabregat-santiago, G. Garcia-Belmonte, J. Bisquert, A. Zaban and P. Salvador, *J. Phys. Chem. B*, 2002, **106**, 334–339.
- 57 J. Bisquert, F. Fabregat-Santiago, I. Mora-Seró, G. Garcia-Belmonte, E. M. Barea and E. Palomares, *Inorg. Chim. Acta*, 2008, **361**, 684–698.
- 58 J. T. Jacobsson and T. Edvinsson, *J. Phys. Chem. C*, 2012, **116**, 15692–15701.
- 59 B. Klahr, S. Gimenez, F. Fabregat-Santiago, T. Hamann and J. Bisquert, *J. Am. Chem. Soc.*, 2012, **134**, 4294–4302.
- 60 H. Wang, G. Wang, Y. Ling, M. Lepert, C. Wang, J. Z. Zhang and Y. Li, *Nanoscale*, 2012, **4**, 1463–1466.
- 61 R. a. Marcus, *J. Phys. Chem. B*, 1998, **102**, 10071–10077.
- 62 H.-Y. Lee, H. Tanaka, Y. Otsuka, K.-H. Yoo, J.-O. Lee and T. Kawai, *Appl. Phys. Lett.*, 2002, **80**, 1670–1672.